Published by
NIGERIAN SOCIETY OF PHYSICAL SCIENCES
Available online @ https://asr.nsps.org.ng/index.php/asr

African Scientific Reports 4 (2025) 263

African Scientific Reports

Effects of precursors composition on characteristics of organic-inorganic Methyl Ammonium Lead Trihalide Perovskite-based thin films

Simeon Amole[a], Oluwaseun Adedokun[a,b,*], Olusola Akinrinola[a], Olumuyiwa Aderemi Oyekanmi[a,c], Festus Akintunde Ojeniyi[a], Adekunle Kazeem Dauda[d], Ayodeji Oladiran Awodugba[a]

[a]*Department of Pure and Applied Physics, Ladoke Akintola University of Technology, P.M.B 4000, Ogbomoso, Nigeria*
[b]*Nanotechnology Research Group (NANO+), Ladoke Akintola University of Technology, Ogbomoso, Nigeria*
[c]*Department of Physical Science, Niger State Polytechnic, P. M. B 001, Zungeru, Nigeria*
[d]*National Agency for Science and Engineering Infrastructure (NASENI), P. M. B 391, Abuja, FCT Nigeria*

Abstract

Precursors compositional engineering is considered as one of the viable methods of manipulating the characteristics of the mixed halide perovskites. In this research, methyl ammonium lead triiodide perovskites ($CH_3NH_3PbI_3$) was synthesized through solution-based processing and deposited on ITO glass substrates using spin coating method. Additionally, the effects of mixed composition of precursors on the deposited films were evaluated by partial replacement of iodine (I) anion with bromine (Br) on $CH_3NH_3Pb(I_{1-x}Br_x)_3$ perovskite with Br compositions for $x = 0.33$ and $x = 0.66$. The deposited films were characterized using X-ray Diffraction (XRD), Fourier Transform Infrared (FTIR) Spectrometry, Ultraviolet-visible Spectrophotometry, Scanning Electron Microscopy (SEM), Transmission Electron Microscopy (TEM) and Solar Simulator to study the structural, optical, morphological and optoelectronic properties of the films. The average crystallites of ~7.94, ~7.70 and ~7.62 nm were calculated for $CH_3NH_3PbI_3$, methyl ammonium lead diiodide bromide ($CH_3NH_3PbI_2Br$) and methyl ammonium lead iodide dibromide ($CH_3NH_3PbIBr_2$) respectively. In addition, the energy bandgaps of 1.63 eV, 1.91 eV and 1.94 eV were extrapolated for $CH_3NH_3PbI_3$, $CH_3NH_3PbI_2Br$ and $CH_3NH_3PbBr_2I$ respectively. The results from J-V curves show the Jsc values of 9.9, 9.2 and 8.6 $mAcm^{-2}$, FF values of 67.00, 58.20 and 54.2%, Voc values of 0.55, 0.54 and 0.52, and PCE values of 3.50, 3.33 and 3.00% were calculated for $CH_3NH_3PbI_3$, $CH_3NH_3PbI_2Br$ and $CH_3NH_3PbBr_2I$, respectively. The results show that partial replacement of I anion with Br on $CH_3NH_3Pb(I_{1-x}Br_x)_3$ perovskite with Br compositions for $x = 0.33$ and $x = 0.66$ did not improve the functionality of the methyl ammonium lead triiodide perovskite material.

DOI:10.46481/asr.2025.4.1.263

Keywords: Mixed halide perovskites, Organo-metallic perovskites, Energy bandgaps, Crystallites, Morphological properties, Mixed composition

Article History :
Received: 21 November 2024
Received in revised form: 28 January 2025
Accepted for publication: 05 February 2025
Published: 04 March 2025

© 2025 The Author(s). Published by the Nigerian Society of Physical Sciences under the terms of the Creative Commons Attribution 4.0 International license. Further distribution of this work must maintain attribution to the author(s) and the published article's title, journal citation, and DOI.

1. Introduction

The quest for cleaner energy as a result of global warming opened a new chapter for photovoltaic solar cells. This drive has given organic-inorganic methyl ammonium lead trihalide perovskite-based solar cells an edge over the mainstream silicon-based

*Corresponding author Tel. No.: +234-703-119-5750.
Email address: oadedokun@lautech.edu.ng (Oluwaseun Adedokun)

solar cells because of its completely fascinating properties such as two-dimensional electronic conductivities, long charge carrier diffusion length and extensive energy bandgap tuneability [1]. Ever since the first research by Miyasaka *et al.* in 2009 on halide perovskites, preponderance of research activities has been concentrating on the materials' performance and stability [2].

Halide perovskites have the chemical formula ABX_3 where A is typically methyl ammonium ($CH_3NH_3^+$), formamidinium ($HC(NH_2)_2^+$), ethyl ammonium ($CH_3CH_2NH_3^+$), caecium (Cs) or butyl ammonium ($CH_3CH_2CH_2CH_2NH_3^+$), B is lead (Pb^{2+}) or tin (Sn^{2+}), and X is iodine (I^-), bromine (Br^-) or chlorine (Cl^-) [3]. Additionally, the materials can have different chemical formulas, including the well-known Ruddlesden-Popper (RP) phases, such as A_2BX_4, ABX_4 and A_3BX_9. The A cation occupies a cubo-octahedral site shared with twelve X anions, whereas the B cation is stabilized in an octahedral site shared with six X anions [4].

Above and beyond the wide-ranging tuneability in chemical composition, halide perovskites can also be processed easily into quantum-dots, large single crystals and polycrystalline thin films. The functionality of the microstructural features (such as grain size, crystallographic orientations, crystal defects, interfaces, surfaces, and grain boundaries) of halide perovskites are completely very tailorable as the materials are responsive to huge arrays of chemical-, gas-, solution-, gas-, vapor-based processing methods [5].

Colella *et al*. investigated the structural properties of iodide/ chloride mixed-halide perovskites and correlating them with their photovoltaic performances. It was found out that, independent of the component's ratio in the precursor solution, Cl incorporation in an iodide-based structure, is possible only at relatively low concentration levels (below 3−4%) [6]. Cui *et al*. prepared color-tuned perovskite films with chemical formula $CH_3NH_3Pb(I_{1-x}Br_x)_3$ for $x = 0,\ 1,\ 2$ *and* 3. The results showed that the material's performance decreased with increasing Br substitution [7].

Additionally, studies have shown that multiple cation mixed-composition perovskites synthesized via alio- and iso-valent doping strongly affects carrier recombination and potential transport of ionic and molecular species, and thus improve the overall performance. For example, Peter *et al*. have studied $BAI_{0.6}$ $Br_{0.4}$-$Cs_{0.6}MA_{0.4}$ PbI_3 (where BA is n-butyl ammonium, and $BAI_{0.6}$ $Br_{0.4}$ acts as a capping layer [8]. The work showed polycrystalline films with improved crystallites, and thus modified the performance. In another study, Islam *et al*. investigated $Cs_2AgBiBr_6$ where it was confirmed that Ag grains infiltrated in to the grain boundaries, and promoted crystallinity enhancement of the film [9]. Besides, Aitola *et al*. evaluated the effects of bromine doping on $CH_3NH_3Pb(I_{1-x}Br_x)_3$ perovskite for Br compositions ranging from $x = 0$ to $x = 0.1$. The results showed a linear increase of the energy bandgap as the function of bromine concentration [10].

Recent studies have shown that multiple cation mixed-composition can be very effective in accelerating photocarriers and improving material's overall performance though, manipulating the characteristics of organic-inorganic methyl ammonium trihalide perovskites via compositional engineering could be a viable tool for tailoring and attainment of new possibility in the material. So far, partial replacement of I anion with Br on $CH_3NH_3Pb(I_{1-x}Br_x)_3$ perovskite crystal lattice is limited to Br compositions for the values of $x < 0.33$. Therefore, there is a crucial need to evaluate the influence of partial replacement of I anion with Br on $CH_3NH_3Pb(I_{1-x}Br_x)_3$ with Br compositions for the values $x \geq 0.33$ on the crystal lattice of the organic-inorganic methyl ammonium lead triiodide perovskite material. In this research, the effects of partial replacement of iodine with bromine anion on characteristics of $CH_3NH_3Pb(I_{1-x}Br_x)_3$ perovskite based thin films with Br compositions for $x = 0,\ 0.33$ and 0.66 were investigated.

2. Materials and methods

2.1. Materials

Lead (II) iodide (PbI_2) 98% purity, methyl ammonium iodide (CH_3NH_3I) 98% purity, Lead (II) bromide ($PbBr_2$) 97% purity, dimethyl formamide (DMF) 97% purity, methyl ammonium bromide (CH_3NH_3Br) 97% purity, isopropanol ($CH_3CH(OH)CH_3$) 99% purity, ethanol (CH_3CH_2OH) 99% purity, Indium doped Tin Oxide (ITO) glass substrates were bought from commercial suppliers (Sigma-Aldrich).

2.2. Synthesis of methyl ammonium lead triiodide ($CH_3NH_3PbI_3$), methyl ammonium lead bromide diiodide ($CH_3NH_3PbBrI_2$) and methyl ammonium lead iodide dibromide ($CH_3NH_3PbIBr_2$) solutions

In this study, solution-based processing in one step was employed to synthesize methyl ammonium lead triiodide, methyl ammonium lead bromide diiodide and methyl ammonium lead iodide dibromide. At first, lead (II) iodide (PbI_2) was preheated for 20 minutes at 60°C to vaporize likely humidity within the salt. In order to synthesized 1 M of $CH_3NH_3PbI_3$, 578 mg of PbI_2 and 200 mg of methyl ammonium iodide (CH_3NH_3I) were dissolved with 1 mL of DMF in a test tube and heated at 250 °C. This temperature was maintained until PbI_2 completely dissolved. The solution was stirred to prevent crystallization of PbI_2. Additionally, 1 M of $CH_3NH_3PbBrI_2$ was synthesized by dissolving 371 mg of lead (II) iodide (PbI_2) and 112 mg of methyl ammonium bromide (CH_3NH_3Br) were mixed in a test tube with 1 mL of DMF and heated 250°C. The solution was then stirred vigorously until PbI_2 dissolves. 1 M of methyl ammonium lead iodide dibromide ($CH_3NH_3PbIBr_2$) solution was prepared by dissolving 371 mg of $PbBr_2$ and 200 mg of methyl ammonium iodide (CH_3NH_3I) in 1 mL of DMF in a test tube and heated at 250 °C. This temperature was maintained until $PbBr_2$ dissolves. The solution was stirred manually to prevent crystallization of $PbBr_2$ [11].

2.3. Deposition of $CH_3NH_3PbBrI_2$, $CH_3NH_3PbBrI_2$ and $CH_3NH_3PbBrI_2$ films

One layer of the synthesized colloidal $CH_3NH_3PbBrI_2$ was spin coated on a cleaned ITO glass slides at 2500 rpm for 20 s, 1000 rpm for 10 s. The spinning speed was varied in order to improve uniformity and coupling fluid rheology of the film. Afterwards, the formed $CH_3NH_3PbBrI_2$ film was allowed dry naturally. The same procedure was employed to deposit colloidal $CH_3NH_3PbBrI_2$ and $CH_3NH_3PbIBr_2$ on cleaned ITO prepatterned glass substrates.

2.4. Characterization of $CH_3NH_3PbBrI_2$, $CH_3NH_3PbBrI_2$ and $CH_3NH_3PbBrI_2$ films

The optical properties such as transmittance, absorbance and wavelength of the devices were acquired from Ultraviolet-visible spectrophotometer (Cary 60, Agilent, USA). X-ray diffraction patterns were obtained with X-ray diffractometer (Rigaku D/Max-lllC, Tokyo, Japan). The instrument was set to produce diffractions at scanning rate of 2 ^{o}/min in the 2 to 50° at room temperature, and CuKa radiation set at 40 kV and 20 mA and40 kV. Scanning electron microscopy (SEM) images were obtained using a JEOL (JSM-6010LV, Tokyo, Japan) microscope. This instrument was set at a working distance of 11 mm and an accelerating voltage of 15 KV. The FTIR spectra were examined using the spectroscopic software Win-FTIR Pro Version 3.0. All spectra were taken from 500 cm^{-1} to 4000 cm^{-1} using the (Pelkin Elmer 3000 MX, Massachusetts, USA) spectrometer. Furthermore, transmission electron microscope (TEM) with JEM-ARM200F-G operating at 300kV. (Keithley 2400, Ohio, USA) source meter under AM 1.5G (1000 Wm^{-2}) solar illumination was used to investigate the devices' performance.

2.5. Theoretical considerations

The absorbance (A), transmittance (T) and reflectance (R) satisfy the law of conservation of energy by the equation [12]:

$$A + R + T = 1, \tag{1}$$

where d is the thickness of the film.

The energy bandgaps of the films were determined by Tauc's relation which is given as [13]:

$$(\alpha \mathrm{h}\nu)^{\frac{1}{n}} = (h\nu - Eg), \tag{2}$$

where h is Plank$^{'}$s constant, α is the coefficient of absorption, ν is frequency (ν $-\frac{c}{\lambda}$ c is the speed of light, λ is the wavelength), n=2 for direct optical band gap, n=$\frac{1}{2}$ for indirect optical band gap, and $E_g$is energy bandgap which is determined by extrapolation of the linear portion to intercept the abscissa.

The optical conductivity (δ) of the perovskite is given by the expression:

$$\delta = \frac{\alpha n c}{4\pi}. \tag{3}$$

The values of extinction coefficient (k) of the perovskite are calculated by the relation:

$$k = \frac{\alpha \lambda}{4\pi}. \tag{4}$$

Thus, the optical dielectricity (ε) of the perovskite is given by the relation [14]

$$\varepsilon = n^2 - k^2. \tag{5}$$

The refractive index (n) of the film is given by the relation [13]:

$$n = \frac{1 + R}{(1 - R) + \left(\sqrt{\frac{4R}{1-R^2-K^2}}\right)}, \tag{6}$$

where λ is the wavelength, π is pi (π =3.142) and n is the refractive index of the film.

The crystallite size (L) was determined from the Scherrer equation [13]:

$$L = \frac{K\lambda}{\beta \mathrm{cosO}}, \tag{7}$$

where O is the one half of peak diffraction angle K is the Scherrer constant (0.9), λ is the wavelength and β is the full width (in radians) of the peak at the half maximum (FWHM) intensity.

Lattice stain (ε) of the materials was calculated by the relation [15]

$$\varepsilon = \frac{\beta \cos\theta}{4}. \tag{8}$$

Table 1: Structural parameters of $CH_3NH_3PbI_3$, $CH_3NH_3PbI_2Br$ and $CH_3NH_3PbIBr_2$ films.

$2\theta(^\circ)$			FWHM(°)			L(nm)			$\delta(nm^{-2}) \times 10^{-2}$			$\varepsilon(\%) \times 10^{-1}$		
$2\theta_1$	$2\theta_2$	$2\theta_3$	β_1	β_2	β_3	L_1	L_2	L_3	δ_1	δ_2	δ_3	ε_1	ε_2	ε_3
28.8	28.9	29.1	1.02	1.02	1.12	8.34	8.39	7.63	1.43	1.42	1.71	2.48	2.47	2.71
34.0	34.2	34.5	1.13	1.12	1.12	7.68	7.75	7.75	1.66	1.66	1.66	2.70	2.67	2.63
40.4	41.6	42.1	1.14	1.15	1.15	7.74	7.68	7.68	1.69	1.69	1.70	2.68	2.70	2.70
50.2	50.4	50.5	1.13	1.15	1.15	8.10	7.91	7.91	1.59	1.59	1.62	2.56	2.62	2.62

θ is the one half of peak diffraction angle or Bragg's angle and ε is the lattice strain.

Stacking fault is calculated by the relation:

$$\alpha = \frac{2\pi^2}{45\sqrt{3tan\theta}} \times \beta. \tag{9}$$

The dislocation density was calculated using the relation [16]:

$$\delta = \frac{1}{L^2}, \tag{10}$$

where α is the stacking fault, δ is the dislocation density and L is the crystallite size.

To calculate the efficiency of a solar cell, the current density of a device is obtained as a function of applied voltage. The efficiency curve gives the parameters necessary to calculate efficiency [17]:

$$\eta = \frac{p_{out}}{p_{in}} = \frac{J_{sc}V_{OC}FF}{p_{in}}, \tag{11}$$

where J_{sc} is the short-circuit current density, P_{out} is the output power of a device η is efficiency and P_{in} the input power of the incident light.

The fill factor is determined by the expression [18]:

$$FF = \frac{J_{mpV_{mp}}}{J_{sc}V_{oc}}, \tag{12}$$

where J_{mp} is the current density of the device at its maximum power, V_{oc} is the open-circuit voltage, FF is the fill factor and V_{mp} is the voltage of the device at its maximum power.

3. Results and discussion

3.1. Study of structural characteristics of synthesized $CH_3NH_3PbI_3$, $CH_3NH_3PbI_2Br$ and $CH_3NH_3Pb\ IBr_2$ halide perovskite films

3.1.1. XRD analysis of synthesized $CH_3NH_3PbI_3$, $CH_3NH_3PbI_2Br$ and $CH_3NH_3Pb\ IBr_2$ halide perovskite films

The XRD patterns of $CH_3NH_3PbI_3$, $CH_3NH_3PbI_2Br$ and $CH_3NH_3PbBr_2I$ films are shown in Figure 1. The results demonstrate that the three materials exhibited similar crystalline structures assignable to perovskite system. Figure 1 displays, for $CH_3NH_3PbI_3$, the dominant absorption peaks at 2θ =28.8°, 32.0, 45.4 and 56.1 which assignable to preferential orientation along (101), (100), (200) and (220) reflections, respectively. The (hkl) indexing was performed with reference to JCPDS card number 41-1445. Compared to $CH_3NH_3PbI_3$ perovskite film, the absorption peaks of $CH_3NH_3PbI_2Br$ and $CH_3NH_3PbBr_2I$ mixed halide perovskite shifted gradually to higher angles as more Br incorporated into $CH_3NH_3PbI_3$ crystal lattice. These variations in (101), (100), (200) and (220) reflections could be rationalized by the shrunken crystalline lattice solely caused by partial replacement of I anion with Br on $CH_3NH_3Pb(I_{1-x}Br_x)_3$ perovskite crystal lattice. In addition, these gradual shifting displacements in the reflections of the perovskite material were attributed to ionic radius of Br anion (1.96 Å) being smaller than the ionic radius of I anion (2.2 Å) [19].

As displayed in Table 1, the average crystallite (L), lattice strain (ε) and dislocation density (δ) of ~7.97 nm, 0.2605% and 0.0159 nm^{-2} were calculated for $CH_3NH_3PbI_3$ compared to ~7.93 nm, 0.2615% and 0.0159 nm^{-2} calculated for $CH_3NH_3PbI_2Br$ and ~7.74 nm, 0.2665% and 0.0167 nm^{-2} calculated for $CH_3NH_3PbIBr_2$. It should be taken into account that Br incorporation into $CH_3NH_3Pb(I_{1-x}Br_x)_3$ perovskite crystal lattice with Br composition for the values of $x \geq 0.33$ reduced the crystallites, and thus increase the concentration of crystal lattice imperfection as a result of the lattice misfit in the films.

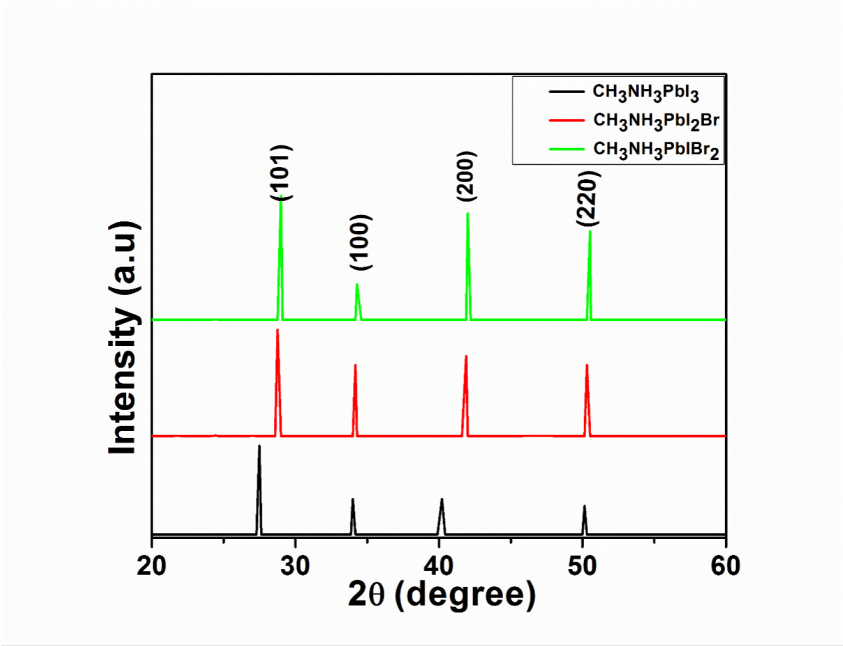


Figure 1: XRD pattern of $CH_3NH_3PbI_3$, $CH_3NH_3PbI_2Br$ and $CH_3NH_3PbBr_2I$ films.

Table 2: Summary of bondtypes and wavenumbers in $CH_3NH_3PbI_3$, $CH_3NH_3PbI_2Br$ and $CH_3NH_3PbIBr_2$ FTIR spectra.

Peak	Wave number (cm^{-1})			Bond type
	$CH_3NH_3PbI_3$	$CH_3NH_3PbBr_2I$	$CH_3NH_3PbI_2Br$	
1	3445.00	3450.00	3492.00	OH stretch
2	3305.00	3305.00	3304.00	N-H stretch
3	2860.00	2932.00	2939.00	CH_3 bend
4	2529.00	2860.00	2862.00	CH_2 bend
5	1742.77	1745.00	1746.77	C=N stretch
6	1460.00	1448.00	1446.00	C-H stretch
7	1065.00	1160.00	1158.00	C-O scissor
8	725.00	671 .00	673.00	C-Br stretch
9	618.00	588.00	589.77	C-I stretch

3.1.2. FTIR analysis of synthesized $CH_3NH_3PbI_3$, $CH_3NH_3PbI_2Br$ and $CH_3NH_3Pb\ IBr_2$ halide perovskite films

Figure 2 presents the FTIR spectra of $CH_3NH_3PbI_3$, $CH_3NH_3PbI_2Br$ and $CH_3NH_3PbBr_2I$ perovskite. The absorption peaks at 3445.00 cm^{-1} and 3305.00 cm^{-1} assignable to OH symmetrical stretching vibration and N-H stretching mode, respectively reduced in $CH_3NH_3PbI_3$ compared to $CH_3NH_3PbI_2Br$ and $CH_3NH_3PbBr_2I$. Additionally, the sharp absorption peak at 1742.77 cm^{-1} which is highly indicative of C=N stretching mode of $CH_3NH_3^+$ cation and the peak at 1657.00 cm^{-1} replying the existence of NH_2 stretching mode. These two absorption peaks undergone right shifting displacements. Furthermore, the absorption peaks situated at 2529.00 cm^{-1} and 2860.00 cm^{-1} which assignable to the asymmetric CH_2 stretching and symmetric CH_3 stretches, respectively experienced right shifting displacements with increasing Br substitution into $CH_3NH_3PbI_3$ crystal lattice. The two absorption peaks located at 618.00 cm^{-1} and 1065.00 cm^{-1} replying the occurrence of C-I and C-O-C stretches, respectively also reduced as Br substitution increased. The shifting displacements of the absorption peaks were due to the partial replacement of I anion with Br on $CH_3NH_3Pb(I_{1-x}Br_x)_3$ perovskite crystal lattice. The degree of displacement increased with increasing Br substitution into $CH_3NH_3Pb(I_{1-x}Br_x)_3$ perovskite crystal lattice. These results agree with the results obtained by Nkele *et al.* [20]. The summary of bondtypes and corresponding wavenumbers in $CH_3NH_3PbI_3$, $CH_3NH_3PbI_2Br$ and $CH_3NH_3PbIBr_2$ FTIR spectra is as shown in Table 2.

3.2. Optical characteristics of $CH_3NH_3PbI_3$, $CH_3NH_3PbI_2Br$ and $CH_3NH_3PbBr_2I$ halide perovskite films

3.2.1. UV/NIR/Vis analysis of $CH_3NH_3PbI_3$, $CH_3NH_3PbI_2Br$ and $CH_3NH_3PbBr_2I$ halide perovskite films

The optical features were acquired by UV-Visible spectrophotometer in Diffuse Reflectance Scattering at ambient temperature between 400 and 800nm to comprehend the energy bandgap and structural band of the synthesized perovskite materials.

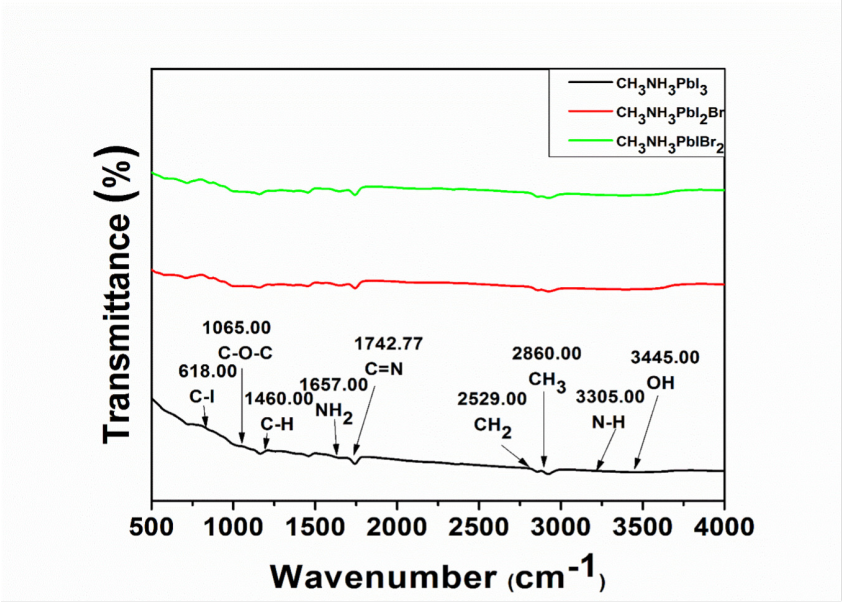


Figure 2: FTIR spectra of $CH_3NH_3PbI_3$, $CH_3NH_3PbI_2Br$ and $CH_3NH_3PbBr_2I$ film showing bond type and wavenumber.

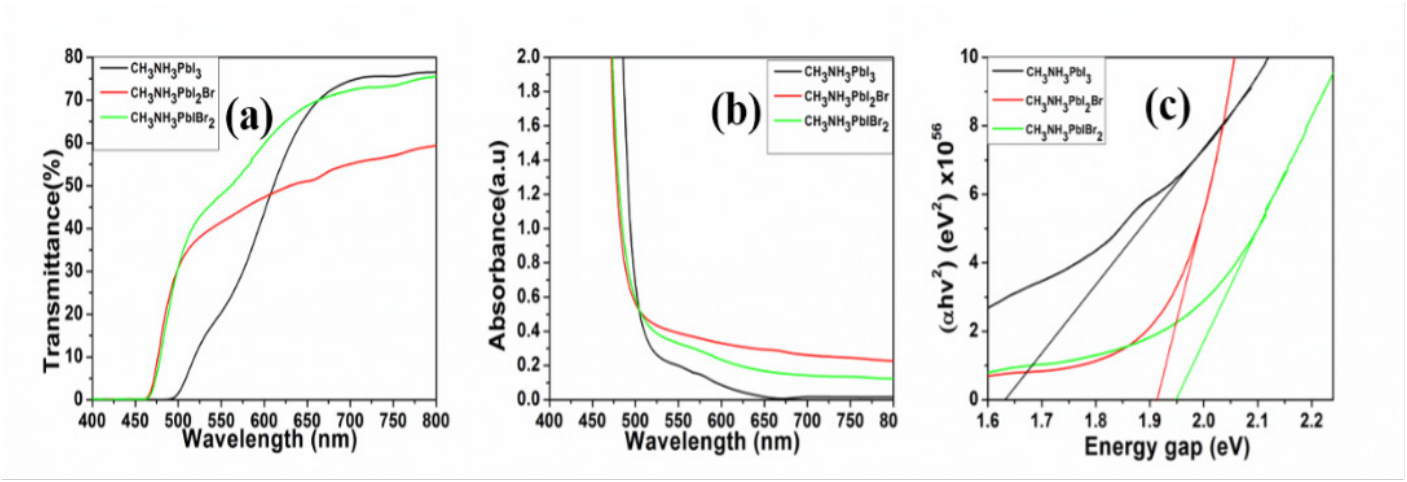


Figure 3: (a) Transmittance-wavelength (b) Absorbance-wavelength (c) $(\alpha hv)^2$ energy gap plots of $CH_3NH_3PbI_3$, $CH_3NH_3PbI_2Br$ and $CH_3NH_3PbIBr_2$ halide perovskite film.

Transmittance-wavelength plots of $CH_3NH_3PbI_3$, $CH_3NH_3PbI_2Br$ and $CH_3NH_3PbBr_2I$ films in Figure 3(a) clearly presents the transmittance onset at around 498 nm for $CH_3NH_3PbI_3$, and 465 nm for $CH_3NH_3PbI_2Br$ and $CH_3NH_3PbBr_2I$ films. The $CH_3NH_3PbI_2Br$ and $CH_3NH_3PbBr_2$ spectra showed enhanced transmittance between the wavelength ranging 485 -500 nm, and steady transmittance within the visible region of solar spectrum with longer wavelength (decreasing photon energy). It should be taken into account that the transmittance onset decreased with increasing Br substitution. These results are consistent with the reports of perovskites with Br dopant observed by Tumen-Ulzii *et al*. [21].

Besides, Br substitution into the perovskite crystal lattice was further evaluated using absorbance-wavelength plot as shown in Figure 3(b). The optical absorption spectra measured and recorded for $CH_3NH_3Pb(I_{1-x}Br_x)_3$ (x = 0.00, 0.33 and 0.66). It worth noting that the maximum absorbance value the synthesized methyl ammonium triiodide decreased with increasing Br substitution with absorption edge located around 650 nm for $CH_3NH_3PbI_3$, and shifted slightly towards lower wavelength (higher photon energy) for $CH_3NH_3PbI_2Br$ and $CH_3NH_3PbBr_2I$ films. This is as result of partial replacement of I anion with Br and modified the band structure and absorption edge of the material [22].

Tauc's plots (Figure 3(c)) were used to estimate the energy bandgaps of $CH_3NH_3PbI_3$, $CH_3NH_3PbI_2Br$ and $CH_3NH_3PbIBr_2$ perovskite films. The plots revealed a blue shift in the energy bandgap of $CH_3NH_3PbI_3$ (1.64 eV). The energy bandgaps of 1.91 eV and 1.95 eV were extrapolated for $CH_3NH_3PbI_2Br$ and $CH_3NH_3PbIBr_2$ perovskites, respectively. It worth noting that the energy bandgap decreased with increasing Br substitution. This is consistent with partial halide replacement in organic-inorganic methyl

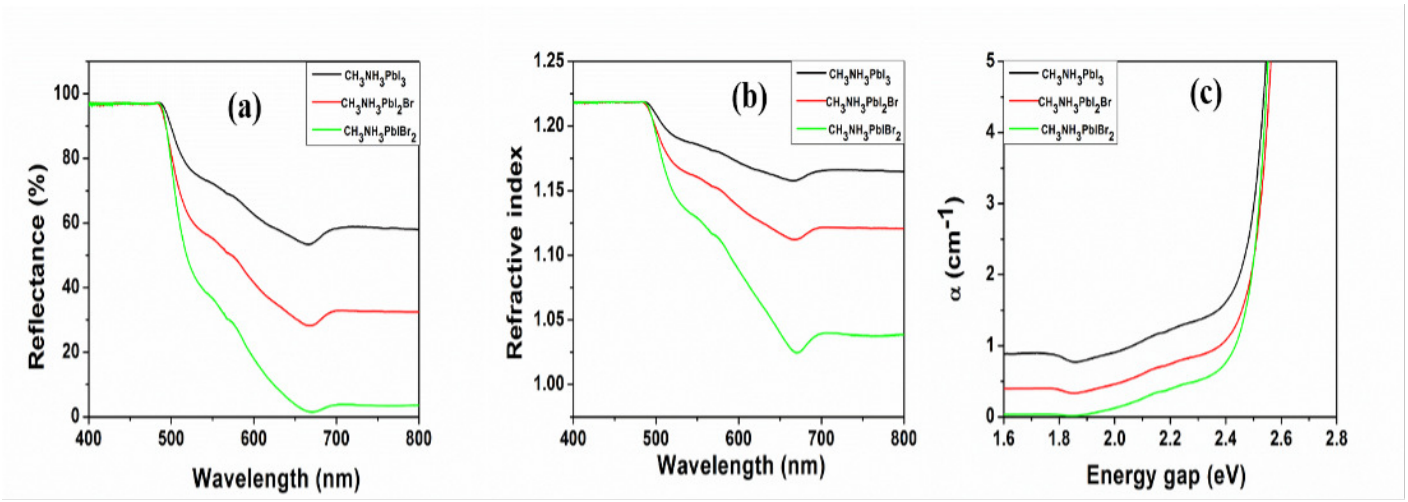


Figure 4: (a) Reflectance-wavelength (b) Refractive index-wavelength (c) absorption coefficient-energy gap plots of $CH_3NH_3PbI_3$, $CH_3NH_3PbI_2Br$ and $CH_3NH_3PbIBr_2$ halide perovskite film.

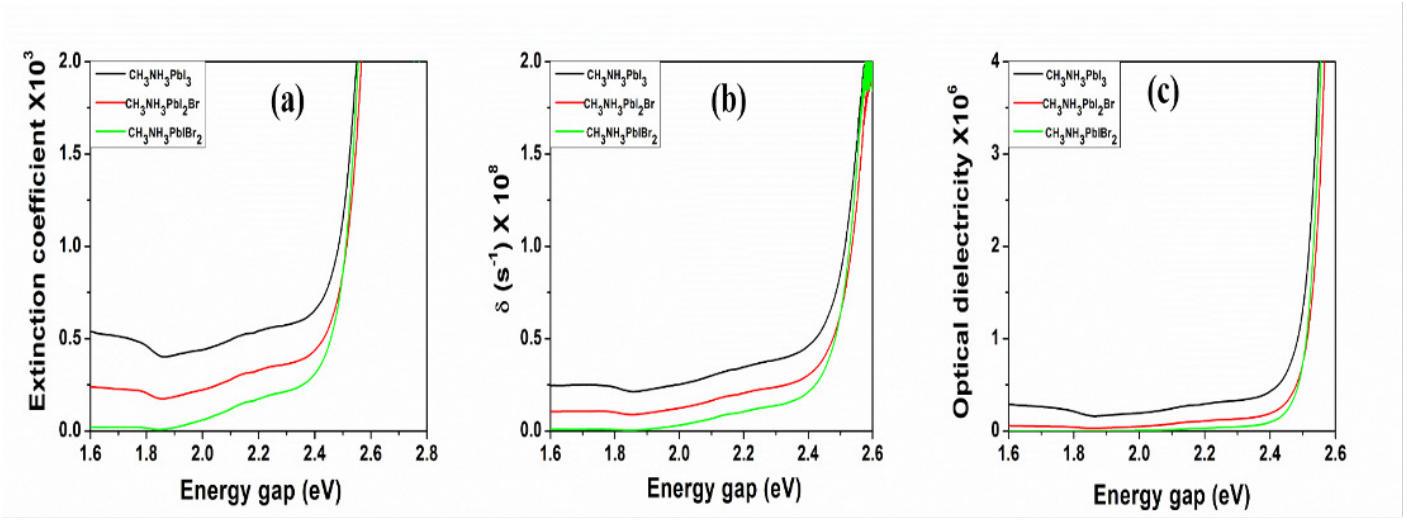


Figure 5: (a) extinction coefficient- energy gap (b) optical conductivity- energy gap (c) optical dielectricity- energy gap plots of $CH_3NH_3PbI_3$, $CH_3NH_3PbI_2Br$ and $CH_3NH_3PbIBr_2$ halide perovskite film.

ammonium lead trihalide perovskite-based films as reported in previous studies [23]. In addition, the blue shift in the energy bandgaps of $CH_3NH_3PbI_2Br$ and $CH_3NH_3PbIBr_2$ compared to $CH_3NH_3PbI_3$ may be due to the variations in crystallite size observed.

Figure 4(a) shows the reflectance-wavelength plots of $CH_3NH_3PbI_3$, $CH_3NH_3PbI_2Br$ and $CH_3NH_3PbBr_2I$ perovskite films. This material showed substantial reflectivity of 96 % at 500 nm, and decreased in towards the longer wavelength ranging 500 nm-800 nm. As seen in Figure 5(a). reflectivity of the perovskite material decreased with increasing partial Br substitution into $CH_3NH_3Pb(I_{1-x}Br_x)_3$ crystal lattice. The decrease in the reflectivity of material was due to different energy formation in the energy bandgap of the synthesized perovskite material. The intensity of reflectivity decreased with increasing Br-substitution.

3.2.2. Linear optical analysis of $CH_3NH_3PbI_3$, $CH_3NH_3PbI_2Br$ and $CH_3NH_3PbBr_2I$ halide perovskite films

Linear optical parameters such as optical dielectricity, refractive index, extinction and absorption coefficients determine the optoelectronic properties of perovskite materials. Refractive index dispersion in Figure 4(b). The figure demonstrates the plot of refractive index with respect to photon energy of the material. There was clear decrease of refractive index with increasing photon energy (decreasing wavelength). As seen from the Figure 4(b), Br substitution into $CH_3NH_3Pb(I_{1-x}Br_x)_3$ crystal lattice improved the refractive index. The refractive index of the perovskite material increased with decreasing wavelength (higher photon energy).

Figure 4(c) shows the spectral dependencies of $CH_3NH_3PbI_3$ films on partial replacement I with Br anion. The absorption coefficient-energy gap plots of $CH_3NH_3PbI_3$, $CH_3NH_3PbI_2Br$ and $CH_3NH_3PbBr_2I$ clearly show similar spectra. They are crucial parameter to characterize the attenuation of light. The values of absorption coefficients decreased at increasing wavelength (lower

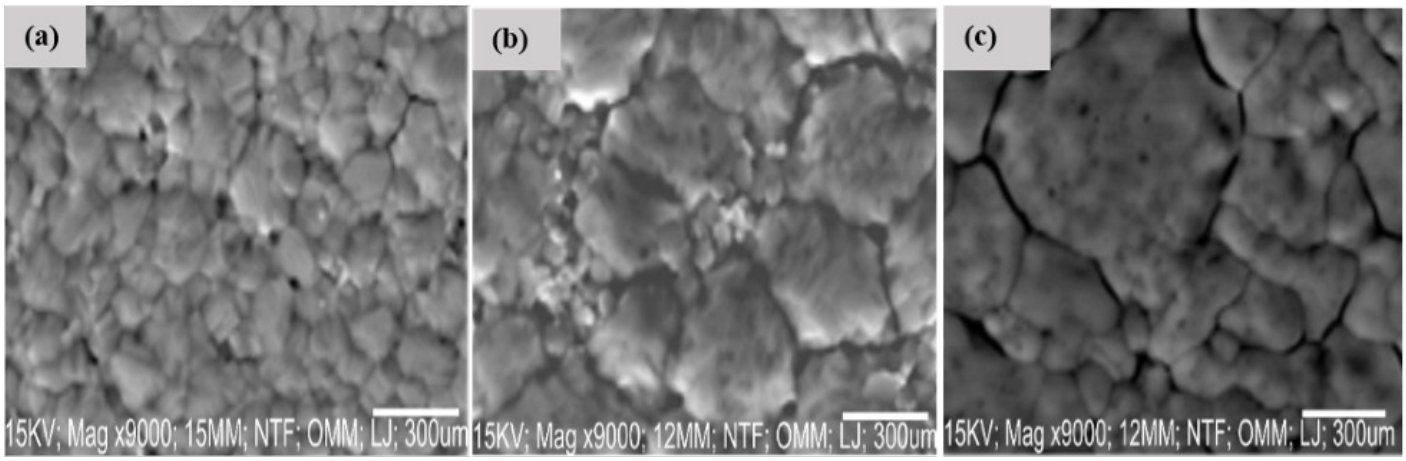


Figure 6: SEM images of (a) $CH_3NH_3PbI_3$ (b) $CH_3NH_3PbI_2Br$ (c) $CH_3NH_3PbIBr_2$ halide perovskite films.

photon energy). The absorption coefficient of $CH_3NH_3PbBr_2I$ film exemplifies increasing behaviour with increasing photon energy (decreasing wavelength). As seen in Figure 4(c), the absorption coefficient of methyl ammonium lead trihalide perovskite films decreased as increasing Br substitution.

Additionally, extinction coefficients as seen Figures 5(a), is related to absorption coefficient. The plots show steady increase in the values of extinction coefficient with decreasing wavelength (increasing in photon energy). Thus, lower values of $CH_3NH_3PbBr_2I$ indicate decreased optical absorption. As observed in Figure 5(a), substantially enhanced extinction coefficient was observed at photon energy of 2.4 eV which is consistent with the values of absorption coefficient obtained in Figure 4(c). It should be noted that the values of extinction coefficient of the synthesized perovskite materials decreased with increasing Br substitution at shorter photon energy (longer wavelength).

Figure 5(b) demonstrates the optical conductivity-energy gap plots of the synthesized $CH_3NH_3PbI_3$, $CH_3NH_3PbI_2Br$ and $CH_3NH_3PbBr_2I$ perovskite films. The plots clearly show similar spectra, and their values increased sharply around the photon energy of 2.5 eV. Additionally, the optical conductivity of the material decreased towards the shorter photon energy (increasing wavelength). As seen in Figure 5(b), the optical conductivity of the perovskite material showed decreasing behaviour with increasing Br substitution in to $CH_3NH_3PbI_3$ crystal lattice. These results agree with previous studies [24]. Figure 5(c) shows the plots of optical dielectricity with photon energy. The plots show steady decrease in the values of optical dielectricity with decreasing in photon energy (increasing wavelength). It was observed that the optical dielectricity of the perovskite material decreased with increasing Br substitution into the $CH_3NH_3PbI_3$ crystal lattice.

3.3. Morphologies of polycrystalline $CH_3NH_3PbI_3$, $CH_3NH_3PbI_2Br$ and $CH_3NH_3PbIBr_2$ halide perovskite films

3.3.1. SEM analysis of polycrystalline $CH_3NH_3PbI_3$, $CH_3NH_3PbI_2Br$ and $CH_3NH_3PbIBr_2$ halide perovskite films

Figures 6(a)-(c) depict the SEM images of $CH_3NH_3PbI_3$, $CH_3NH_3PbI_2Br$ and $CH_3NH_3PbIBr_2$ halide perovskite films. As seen from SEM images, the samples have compact structure, well continuity, homogeneous distribution shapes devoid of disfigurement, and smooth in appearance. No cracks were observed throughout the surface of $CH_3NH_3PbI_3$ and $CH_3NH_3PbI_2Br$ films which is highly indicative of high degree of crystallinity, and the grain boundaries were ubiquitous. However, cracks were observed in the surface of $CH_3NH_3PbIBr_2$ film, which could have resulted due to increasing Br substitution. It is becoming increasingly clear that the occurrence of cracks is fundamentally indicative of reduced crystallinity. As observed from the SEM images, the crystallinity of methylammonium lead trihalide perovskite material decreased with increasing Br substitution.

3.3.2. TEM analysis of polycrystalline $CH_3NH_3PbI_3$, $CH_3NH_3PbI_2Br$ and $CH_3NH_3PbIBr_2$ halide perovskite films

Figures 7(a)-(c) displayed the corresponding TEM images of $CH_3NH_3PbI_3$, $CH_3NH_3PbI_2Br$ and $CH_3NH_3PbIBr_2$ halide perovskite films. The Figure clarifies the full formation mechanism of perovskite particles from solutions occur at the nanometers length scales by which crystallization and crystallite growth take place. The halide perovskites particles were formed through direct nucleation of the crystals from supersaturated CH_3NH_3Br and PbI_2 precursor solutions [24]. It is important to note that the TEM images show some degree of density in the cluster of nearly spherical nanoparticles which decreased with increasing Br substitution into to $CH_3NH_3Pb(I_{1-x}Br_x)_3$ perovskite crystal lattice. No aggregation and coalescence of the nanoparticles was found in $CH_3NH_3PbI_3$ nanoparticles, indicating that the ligands at the nanoparticle surface was able to give rise to sufficient steric force to enable well-separated nanoparticles. Nonetheless, $CH_3NH_3PbI_2Br$ and $CH_3NH_3PbIBr_2$ nanoparticles seemed to coalesce and aggregate with increasing Br substitution. As can be seen, the aggregation and coalescence of the nanoparticles was more prominent with

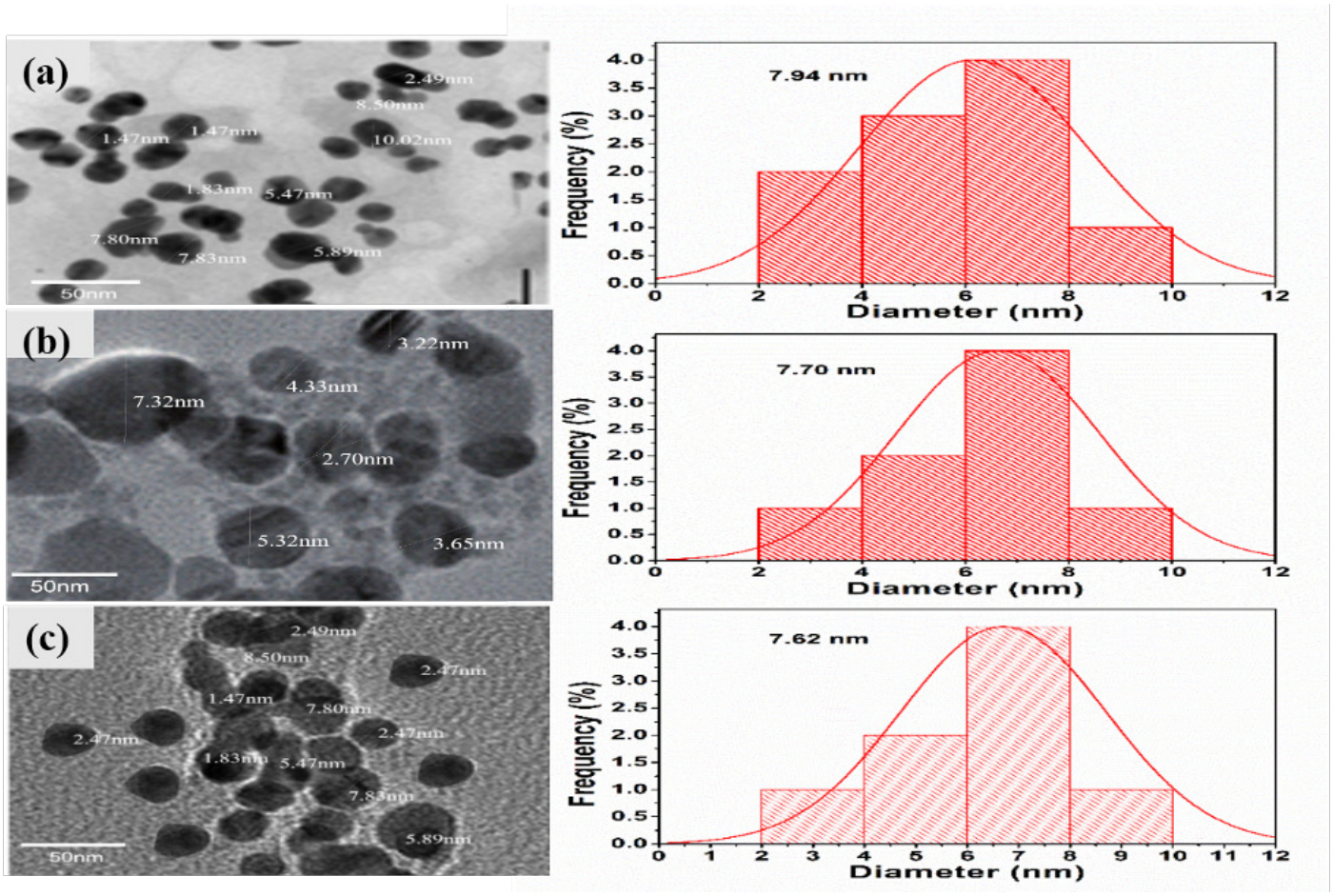


Figure 7: TEM images of (a) $CH_3NH_3PbI_3$ (b) $CH_3NH_3PbI_2Br$ (c) $CH_3NH_3PbIBr_2$ halide perovskite films.

Table 3: Photovoltaic performance comparison of $CH_3NH_3PbI_3$, $CH_3NH_3PbI_2Br$ and $CH_3NH_3PbIBr_2$ halide perovskite films.

Films	Archetecture	J_{SC} $(mAcm^{-2})$	$V_{OC}(V)$	$FF(\%)$	$PCE(\%)$
1	$CH_3NH_3PbI_3$	9.9	0.55	67.99	3.50
2	$CH_3NH_3PbI_2Br$	9.2	0.54	58.26	3.00
3	$CH_3NH_3PbBr_2I$	8.6	0.52	54.20	2.71

Br on $CH_3NH_3Pb(I_{1-x}Br_x)_3$ perovskite with Br compositions for $x = 0.66$. The average particle size of 7.94, 7.70 and 7.62 nm were calculated for $CH_3NH_3PbI_3$, $CH_3NH_3PbI_2Br$ and $CH_3NH_3PbIBr_2$, respectively, which consistent with XRD results.

3.4. Photovoltaic evaluation of synthesized $CH_3NH_3PbI_3$, $CH_3NH_3PbI_2Br$ and $CH_3NH_3PbIBr_2$ films

The performance evaluation of photovoltaic parameters such as Voc, Jsc, FF and PCE were obtained from the J-V curves of $CH_3NH_3PbI_3$, $CH_3NH_3PbI_2Br$ and $CH_3NH_3PbIBr_2$ halide perovskite films, respectively, as shown in Figure 8. As portrayed in Table 3, Br substitution into the methyl ammonium lead triiodide perovskite crystal lattice generated decreased values of V_{OC} from 0.55 V to 0.54V, Jsc values from 9.9 $mAcm^{-2}$ to 9.2 $mAcm^{-2}$, FF values reduced from 67.0 % to 58.2 % and PCE values decreased from 3.50% to 3.00% with Br substitution on $CH_3NH_3Pb(I_{1-x}Br_x)_3$ perovskite with Br compositions for the value of $x = 0.33$. Additionally, Br substitution into the methyl ammonium lead triiodide perovskite crystal lattice produced reduced values of Jsc from 9.9 $mAcm^{-2}$ to 8.6 $mAcm^{-2}$, V_{OC} values from 0.55 V to 0.52V, FF values from 67.0 % to 54.2 % and PCE decreased from 3.50% to 2.71% with Br substitution on $CH_3NH_3Pb(I_{1-x}Br_x)_3$ perovskite with Br compositions for the value of $x = 0.66$.

The reduction in the values of Jsc, FF and PCE of $CH_3NH_3PbI_2Br$ and $CH_3NH_3PbIBr_2$ perovskite was due to decreased extraction and transportation of charged carriers, and increased the possibility of non-radiative recombination rate induced in $CH_3NH_3PbI_2Br$ and $CH_3NH_3PbIBr_2$ crystal lattice, and thus reduced the photovoltaic responses of the perovskite materials. In addition, the reduction in the values of Voc in the perovskite films could be as a result of hysteresis effect in the perovskite films owing to increase in the concentration of lattice misfit present in the films [25].

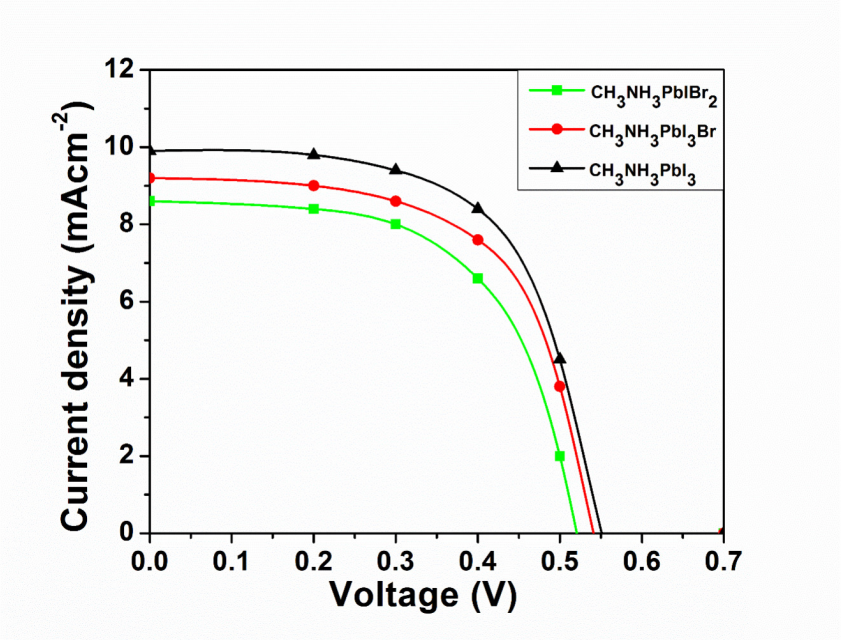


Figure 8: J-V curves of $CH_3NH_3PbI_3$, $CH_3NH_3PbI_2Br$ and $CH_3NH_3PbIBr_2$ halide perovskite films.

4. Conclusion

In this research, $CH_3NH_3PbI_3$, $CH_3NH_3PbI_2Br$ and $CH_3NH_3PbBr_2I$ colloids were synthesized using solution -based processing and deposited on ITO glass substrates via spin coating technique. Characterization studies were carried out on the deposited films. The average crystallites of ~7.97, ~7.93 and ~7.74 nm were calculated for $CH_3NH_3PbI_3$, $CH_3NH_3PbI_2Br$ and $CH_3NH_3PbBr_2I$ respectively relative to the average particle sizes of ~7.94, ~7.70 and ~7.62 nm calculated for $CH_3NH_3PbI_3$, $CH_3NH_3PbI_2Br$ and $CH_3NH_3PbBr_2I$ respectively, from TEM results. Additionally, the energy bandgaps of 1.63 eV, 1.91 eV and 1.94 eV were extrapolated for $CH_3NH_3PbI_3$, $CH_3NH_3PbI_2Br$ and $CH_3NH_3PbBr_2I$ respectively. The results from J-V curves demonstrate the Jsc values of 9.9, 9.2 and 8.6 $mAcm^{-2}$, FF values of 67.00, 58.20 and 54.2%, Voc values of 0.55, 0.54 and0.52, and PCE values of 3.50, 3.33 and 3.00% were calculated for $CH_3NH_3PbI_3$, $CH_3NH_3PbI_2Br$ and $CH_3NH_3PbBr_2I$, respectively. The study demonstrates that partial replacement of I anion with Br on $CH_3NH_3Pb(I_{1-x}Br_x)_3$ perovskite with Br compositions for the value of $x \geq 0.33$ reduced the photovoltaic response of methyl ammonium lead triiodide perovskite material. Br substitution $CH_3NH_3Pb(I_{1-x}Br_x)_3$ can improve the perovskite crystallization, increase photovoltaic performance, and reduce the possibility of non-radiative recombination rate by passivation of the crystal grain boundaries. Future research should focus on optimizing bromine incorporation through techniques like gradient composition and doping to improve device efficiency and explore potential applications in high-efficiency solar cells, LEDs, and photodetectors.

Data availability

Data will be made available by the corresponding author upon request.

Acknowledgement

The authors gratefully acknowledge the technical supports of the Engineering Management Development Institute (EMDI), Akure, Material Science and Engineering Laboratory, KWASU, Malete, and Industrial Laboratory, Pure and Applied Chemistry Department, LAUTECH, Ogbomoso.

References

[1] Q. Wang, Q. Dang, T. Li, A. Gruvaman & J. Hasung, "Thin insulating tunneling contact for efficient and water resistant perovskite solar cells", Ad. Mater. **28** (2024) 6734. https://doi.org/10.1002/adma.201600969.

[2] T. Miyasaka, T. Singh & M. Ikegami, "Ambient fabrication of 126μm thick complete perovskite photovoltaic device for high flexibility and performance", ACS Applied Energy Materials **1** (2018) 6741. https://doi.org/10.1021/acsaem.8b01623.

[3] A. C. Nkele, U. Nwanko, A. Alshoaibiu & F. I. Ezema, "One step spin coating of methylammonium lead iodide on SILAR-deposited tin oxide (SnO_2) for effective electron transport", Results in Optics **13** (2023) 100521. https://doi.org/10.1016/j.rio.2023.100521.

[4] N. G. Park, "Perovskite solar cells: an emerging photovoltaic technology", Mater. Today **18** (2015) 65. https://doi.org/10.1016/j.mattod.2014.07.007.

[5] Z. L. Zhao, N. L. Tran, Y. L. Lin, S. H. Silver, R. A. Kerner, N. Yao, A. Kahn, G. D. Scholes & B. P. Rand, "Mixed-halide perovskites with stabilized bandgaps", Nano Lett. **17** (2017) 6863. https://doi.org/10.1021/acs.nanolett.7b03179.

[6] S. Colella, E. Mosconi, P. Fedeli, A. Listorti, F. Gazza, F. Orlandi, P. Ferro, T. Besagni, A. Rizzo, G. Calestani, G. Gigli, F. De Angelis & R. Mosca, "$MAPbI_{3-x}Cl_x$ mixed halide perovskite for hybrid solar cells: the role of chloride as dopant on the transport and structural properties", Chem. Mater. **25** (2013) 4613. https://doi.org/10.1021/cm402919x.

[7] D. Cui, Z. Yang, X. Ren, Y. Liu, Q. Wei, H. Fan, J. Zeng & S. Liu, "Color-tuned perovskite films prepared for efficient solar cells applications", J. Phys. Chem. **120** (2016) 42. https://doi.org/10.1021/acs.jpcc.5b09393.

[8] J. H. Peter, C. Arthur, W. J. Eurig & P. K. Christopher, "Metal oxide oxidation catalyst as scaffold for perovskite solar cells", Materials (Basel) **13** (2020) 949. https://doi.org/10.3390/ma13040949.

[9] M. Islam, K. Yuyama, K. Takahashi, T. Nakamura, K. Konishi & V. Biju, "Mixed halide perovskite synthesized by chemical reaction and crystal nucleation under optical potential", NPG Asia Materials **11** (2019) 31. https://doi.org/10.1038/s41427-019-0131-0.

[10] K. Aitola, K. Domanski, J. P. Correa-Baena, K. Sveinbjornsson, M. Saliba, A. Abate, M. Gratzel, E. Kauppinon, E. M. J. Johansson, W. Tress W, A. Hagfeldt & G. Boschloo, "High temperature-stable perovskite solar cell based on low-cost carbon nanotubehole contact", Adv. Mater. **17** (2019) 1606398 https://doi.org/10.1002/adma.201606398.

[11] S. Amole, O. Adedokun, O. Akinrinola, M. K. Awodele, F. A. Ojeniyi, O. A. Oyekanmi & A. O. Awodugba, "Improved performance efficiency of manganese dioxide nanoparticles passivated perovskite solar cells", Journal of Material Science: Materials in Electronics **36** (2025) 38. https://doi.org/10.1007/s10854-024-14104-z.

[12] M. Hu, C. Bi, Y. Yuan, Y. Bai & J. Huang, "Stabilized wide bandgap $MAPbBr_xI_{3-x}$ perovskite by enhanced grain size and improved crystallinity", Adv. Sci. **3** (2015) 1500301. https://doi.org/10.1002/advs.201500301.

[13] R. D. Chavan, D. Prochowicz, B. Bończak, M. M. Tavakoli, P. Yadav, M. Fiałkowski & C. K. Hong, "Gold nanoparticlesfunctionalized with fullerene derivative as an effective interface layer for improving the efficiency and stability of planar perovskite solar cells", Adv. Mater. Interfaces. **7** (2020) 2001144. https://doi.org/10.1002/admi.202001144.

[14] D. Cui, Z. Yang, D. Yang, X. Ren, Y. Liu, Q. Wei, H. Fan, J. Zeng & S. Liu, "Colored- tuned perovskite films prepared for efficient solar cells", Applications J. Phys. Chem. **120** (2016) 42. http://doi.org/10.1021/acsjpcc.5b09393.

[15] A. C. Nkele, A. C. Nwaya, N. M. Shainde, S. Ezugwu, M. Maaza, J. S. Shaiku & F. I. Ezema, "The use of nickel oxide as a hole transport material in perovskite solar cells centrifugation: achieving a high performance and stable device", International Journal of Energy Research **44** (2020) 9839. https://doi.org/10.1002/er5563.

[16] M. Ipsita, S. Mangal, S. Jana & P. Singh, "Post annealing effect of perovskite ($CH_3NH_3PbI_3$) thin film for solar cell application", **2369** (2021) 020046. https://doi.org/10.1063/5.0061270.

[17] W. Ke, D. Zhao, A. Cimaroli, C. Grice, P. Qin, Q. Liu, L. Xiong, Y. Yan & G. Fang, "Effect of annealing temperature of tin oxide electron selective layers on the performance of perovskite solar cells", Journal of Materials Chemistry **3** (2015) 24163. https://doi.org/10.1039/C5TA06574G.

[18] S. Amole, O. Adedokun, O. Akinrinola, O. A. Oyekanmi, F. A Ojeniyi, A. K. Dauda & A. O. Awodugba, "Influence of post thermal treatment on characteristics of polycrystalline hybrid perovskite nanoparticle thin films", Sustainable Energy Research **11** (2024) 30. https://doi.org/10.1186//540807-24-00124-0.

[19] S. Amole, M. Awodele, O. Adedokun, M. Jain & A. O. Awodugba, "Sol-gel spin coating synthesis of TiO_2 nanostructure and its optical characterization", Journal of Material Science and Chemical Engineering **7** (2019) 23. http://doi.org/10.4236/msce2019.76003.

[20] A. C. Nkele, A. C. Nwanya, N. M. Shinde, S. Ezugwu, M. Maaza, J. S. Shaiku & F. I. Ezema, "The use of nickel oxide as a hole transport material in perovskite solar cell centrifugation: achieving a high performance and stable device", International Journal of Energy Research **44** (2020) 9839. https://doi.org/10.1002/er.5563.

[21] G. Tumen-Ulzii, C. Qui, P. Leyden, P. Wang, M. Auffray, T. Fujihara, T. Matsushima, J. W. Lee, S. J. Lee, Y. Yang & C. Aucachi, "Detrimental effect of unreacted PbI_2 on long term stability of perovskite solar cells", Ad. Mater. **32** (2020) 1905035. https://doi.org/10.1002/adma.201905035.

[22] H. Mehdi, A. Ahamdi, R. Hannachi & A. Bouazizi, "$MAPbBr_3$ perovskite solar cells via a two-step deposition process", RSC Adv. **9** (2019) 12906. https://doi.org/10.1039/c9ra02036e.

[23] S. Zhou, "Rapid separation and purification of lead halide perovskite quantum dots through differential in nonpolar solvent", RSC Adv. **11** (2021) 28410. https://doi.org/10.1039/d1ra04578d.

[24] M. Otonicar, S. D. Skapin, B. Jancar, R. Ubic & D. Suvorov, "Analysis of the phase transition and the domain structure in $K_{0.5}Bi_{0.5}TiO_3$ perovskite ceramics by in situ XRD and TEM", J. Am. Ceram. Soc. **93** (2010) 4168. https://doi.org/10.1111/j.1551-2916.2010.04013.x.

[25] Y. Zhou, H. Sternlicht & N. P. Padture, "Transmission electron microscopy of halide perovskite materials and devices", Joule **3** (2019) 641. https://doi.org/10.1016/j.joule.2018.12.011.